Low temperature molten salt synthesis of CeF_3 and $CeF_3:Tb^{3+}$ phosphors with efficient luminescence properties

Xuejiao Li*, Wanqi Zhang, Limin Dong, Dongyue Liu, Zhigang Qi

College of Materials Science and Engineering, Harbin University of Science and Technology, Harbin 150040, China

ABSTRACT

CeF_3 and $CeF_3:Tb^{3+}$ particles have been successfully synthesized in a low temperature by the facile molten salt synthesis (MSS) method using $NaNO_3$ and KNO_3 as the reaction medium. The phase, morphology, photoluminescence and cathodoluminescence properties of the samples were investigated systematically. The substitution of Tb^{3+} ions in the CeF_3 lattice has a significant influence on the phase, microstructure and photoluminescent intensity. The emission intensity of $CeF_3: Tb^{3+}$ increases with the concentration of Tb^{3+}, reaching a maximum at 20%Tb mol. The excitation peaks suggest the energy transfer from Ce^{3+} to Tb^{3+}, and the maximal energy transfer rate is estimated to be 98.2%. Under the excitation of the low voltage electron beams, the $CeF_3:Tb^{3+}$ phosphor shows the characteristic emissions of Tb^{3+} which is similar to the photoluminescence properties. The outstanding luminescence properties make the as-obtained samples highly potential in displays, sensors and telecommunications.

1. Introduction

Nature's ability of forming numerous inorganic features which are perfectly adapted for their desired functions has inspired substantial research in materials science [1,2]. Rare-earth (RE) ions substituted inorganic luminescent materials have been extensively researched due to the fascinating optical characteristic and stability [3,4], which are highly potential in the fields of light-emitting diodes (LEDs), cathode ray tubes (CRTs), field-emission displays (FEDs), vacuum fluorescent displays (VFDs), plasma display panels (PDPs), and X-ray imaging scintillators [5–7]. The interesting chemical and photophysical properties of the RE^{3+} dopants is mainly caused by the unique $4f^N$ (N = 1–14) electronic configurations, which are well shielded by the outer 5s and 5p orbitals, leading the sharp and narrow emission bands and thus generating individual colors in multi-phosphor devices [8,9]. In particular, rare-earth fluorides have been extensively reported as an excellent host matrix for down-conversion (DC) and up-conversion (UC) processes due to the good coordination capability, high refractive index, and low phonon energy [10,11].

As a category of important rare-earth fluorides, binary fluoride REF_3 structures have attracted much attention because of their extra high density, fast response, and high- radiation resistance with potential applications in optics, optoelectronics, and fluorescent labeling [12–14]. As a typical example of the binary fluorides, CeF_3 possesses a

hexagonal phase structure with $P\bar{3}|c1$ (D_{3d}^4) space group and six molecules comprised in the unit cell [15]. The Ce^{3+} ion in the CeF_3 crystal is coordinated by nine F⁻ and has a C_2 site symmetry. Additionally, CeF_3 possess larger Stokes shift (10,000 cm^{-1}) as a luminescent material with 100% activator concentration [16]. This large stokes shift value and the resultant smaller spectral overlap prevent resonant energy transfer among Ce^{3+} ions, thus decreasing the probability of concentration quenching by energy migration. Furthermore, CeF_3 has high quantum efficiency and broad emission spectrum in the ultraviolet (UV) region at room temperature, which makes it quite suitable for development of tunable and short-pulsed solid state lasers in this spectral region [17]. Particularly, Ce^{3+} ions with optically allowed d–f transitions exhibit a larger absorption in the UV region and a shorter luminescence life time as an excellent sensitizer [18–20]. Tb^{3+} is an excellent emitter for green emissions and has been widely used for green phosphors for lighting and biological label [21–23]. Doping Tb^{3+} in CeF_3 results in a strong green emission due to the high-efficiency energy transfer from Ce^{3+} to Tb^{3+}, which is observed in the Ce^{3+} and Tb^{3+} co-doped materials such as $LaPO_4$ and $NaYF_4$ phosphors [24–26]. So far, a variety of strategies have been designed for the synthesis of CeF_3 and $CeF_3:Tb^{3+}$ phosphors including polyol process, hydrothermal method, ultrasound route, micro-emulsion approach, electrospray technique, and the thermolysis process [27–30].

However, the synthesis methods mentioned above are restricted by

---

the large-scale preparation or complicated technology/equipment. Moreover, the development of mass production and environmentally friendly synthetic methods is of paramount importance for realizing the full potential of these materials. The molten-salt synthesis (MSS) method is one of the simplest, cost-effective approaches available for obtaining highly crystalline, chemically purified, single phase materials and often in overall short reaction time with little residual impurities [31–33]. These molten salts are usually used as a highly reactive medium which has higher oxidizing potential, high mass transfer, high thermal conductivity, as well as relatively lower viscosities and densities [34]. In this paper, a facile molten salt method has been developed to fabricate CeF_3 and $CeF_3:Tb^{3+}$ phosphors in a short reaction time using $NaNO_3$–KNO_3 as molten salt medium, which provide homogeneous fluid phase in the crystalline phase of metal fluorides. The optical properties of as-obtained fluorides under UV light and low voltage electron excitation were well investigated. The development of molten salt route will serve as the complementary method of previous studies and open up the possibility to meet the increasing commercial demand. Furthermore, the unique luminescence properties of CeF_3 and $CeF_3:Tb^{3+}$ phosphors make these crystals promising for applications in display, sensors and telecommunications.

2. Experimental section

2.1. Materials and synthesis

Tb_4O_7 and $Ce(NO_3)_3 \cdot 6H_2O$ (99.99%) were purchased from Sinopharm Chemical Reagent Co., Ltd, China. $Tb(NO_3)_3$ was prepared by dissolving Tb_4O_7 in dilute HNO_3 solution at elevated temperature followed by evaporating superfluous HNO_3 and the solvent under vacuum. Other chemicals were analytical-grade reagents purchased from Beijing Chemical Corporation.

In a typical synthesis for CeF_3, stoichiometric amounts of $Ce(NO_3)_3 \cdot 6H_2O$, NaF, $NaNO_3$, KNO_3 with molar ratio of 1:3:50:25 were thoroughly mixed with an appropriate amount of ethanol in an agate mort and ground for 30 min. This mixture was then transferred to an alumina crucible and heated to 350 °C and kept at this temperature for 4 h. After cooling down to room temperature, the product was obtained by washing with deionized water for several times, and dried at 100 °C overnight. $CeF_3:Tb^{3+}$ sample was prepared through a similar process except for adding different amount of Tb^{3+}. We can easily and routinely scale up this process to produce large amounts of CeF_3 and $CeF_3:Tb^{3+}$ phosphors. For comparison, bulk CeF_3 phosphors were prepared by solid state reaction and annealed at 800 °C for 6 h.

2.2. Characterization

X-ray powder diffraction (XRD) measurements were performed on a Rigaku TTR III diffractometer at a scanning rate of 10°/min in the 2θ range from 10° to 80°, with graphite monochromatic Cu Ka radiation (λ = 0.15405 nm). X-ray photoelectron spectra (XPS) were taken on a VG ESCALABMK II electron energy spectrometer using Mg KR (1253.6 eV) as the X-ray excitation source. SEM micrographs were obtained using a field emission scanning electron microscope (FE-SEM, S-4800, Hitachi). Transmission electron microscopy (TEM) and high-resolution transmission electron microscopy (HRTEM) images were recorded using a FEI Tecnai G^2 S-Twin with a field emission gun operating at 200 kV. Images were acquired digitally on a Gatan multiple CCD camera. The photoluminescence (PL) measurements were recorded with a Hitachi F-7000 spectrophotometer equipped with a 150 W xenon lamp as the excitation source. The cathodoluminescence (CL) measurements were conducted in an ultra-high-vacuum chamber ($< 10^{-8}$ Torr), where the phosphors were excited by an electron beam at a voltage range of 2–6 kV with different filament currents 80–96 mA, and the spectra were recorded using an F-7000 spectrophotometer. All the measurements were performed at room-temperature (RT).
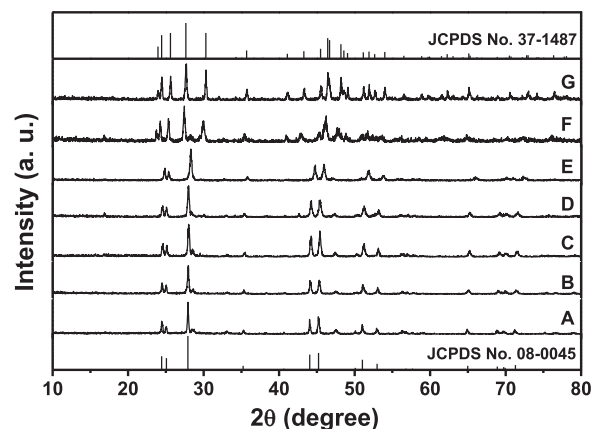
Fig. 1. XRD patterns of as-prepared CeF_3 (A), $CeF_3:5\%Tb^{3+}$ (B), $CeF_3:10\%Tb^{3+}$ (C), $CeF_3:20\%Tb^{3+}$ (D), $CeF_3:40\%Tb^{3+}$ (E) $CeF_3:80\%Tb^{3+}$ (F), and pure TbF_3 (G). The standard data for CeF_3 (JCPDS No. 08–0045) and TbF_3 (JCPDS No. 37–1487) are shown as references.

3. Results and discussion

3.1. Phase, morphology and structure

The composition and phase purity of the as-prepared samples were first investigated by XRD. Fig. 1A shows the typical XRD patterns of the as-obtained CeF_3, which can be well indexed to the hexagonal phase of bulk CeF_3 with cell constants of a = 7.112 and c = 7.279 (JCPDS No. 08–0045; space group: $P6_3/mcm$ (193)). No impurity peaks can be detected, indicating the pure phase of CeF_3 under such experimental conditions. Fig. 1B-E show the XRD patterns of $CeF_3:5\%Tb^{3+}$, $CeF_3:10\% Tb^{3+}$, $CeF_3:20\%Tb^{3+}$, $CeF_3:40\%Tb^{3+}$ samples, respectively. All four samples exhibit the characteristic peaks of pure hexagonal CeF_3 except for a right shift. Considering that the ionic radii of Tb^{3+} is smaller than that of Ce^{3+}, it is natural that the crystal lattice shrinks to some extent and causes the diffraction signals shift to higher degree [20]. The shrink of the lattice constants and the peak shifts as a function of the Tb^{3+} ion concentration indicate that the Tb^{3+} have been effectively built into the CeF_3 host lattice by substituting Ce^{3+}. As for $CeF_3:80\%Tb^{3+}$ (Fig. 1F), the diffraction peaks are basically consistent with orthorhombic TbF_3 phase (JCPDS No. 37–1487) apart from several small peaks of CeF_3 phase. Pure TbF_3 sample with high crystallinity can also been obtained under the same conditions when the doping concentration of Tb^{3+} ions is 100 mol% (Fig. 1G).

In the process of synthesis of CeF_3 phosphors, $NaNO_3$-KNO_3 was used as a molten salt medium. However, such a medium is strong oxidizing due to the existence of NO_3^- which may oxidizes Ce^{3+} partially to Ce^{4+}. In order to solve the problem, we used N_2 protective atmosphere to protect the system. To further confirm the absence of Ce^{4+}, the CeF_3 phosphor is subjected to XPS analysis and shown in Fig. 2. XPS is a very useful analytical technique for investigating the elementary states on the surfaces. The binding energies at 883.1 and 903.3 eV are attributed to Ce $3d_{5/2}$ and $3d_{3/2}$ peaks, respectively. The binding energy at 685.7 eV is attributed to the F peaks. The oxygen and carbon detected in the XPS measurement may come from the atmosphere. Furthermore, low amounts of oxygen and carbon are frequently observed in the XPS spectra. No peaks from the Ce^{4+} are detected indicted no Ce^{4+} exist in the system.

As illustrated before, doping is of fundamental importance in stabilizing the crystallographic phase, size of the products [1]. Thus, high concentration of Tb^{3+} in CeF_3 nanocrystals should greatly influence the morphologies and sizes of the samples. Fig. 3 depicts the representative SEM images of $CeF_3:xTb^{3+}$ with different Tb^{3+} concentration. In Fig. 3A, the as-prepared sample without doping Tb^{3+} ion (pure CeF_3) consists of numerous hexagonal prisms with the size of 50–300 nm and
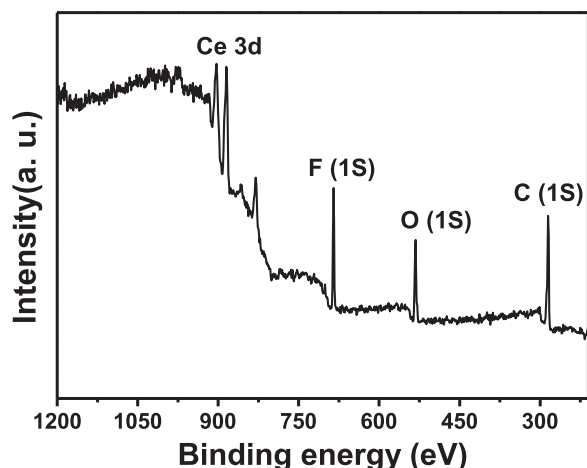
Fig. 2. XPS spectra of CeF$_3$.

some small cubic nanoparticles. The hexagonal microprisms occupy most of the product. When the Tb^{3+} concentration is increased to 5 mol % (Fig. 3B) and 40 mol% (Fig. 3C), and the morphology evolution as a ranging from 60 to 300 nm and small amount of hexagonal micro/prisms are obtained. With further increasing the Tb^{3+} content to 100% (pure TbF$_3$), some octahedrons are achieved (Fig. 3D). Close observation of the image reveals that most of the small particles are still octahedral-like which are similar to the large one except for different particle size. A possible phase and morphology evolution mechanism is proposed in Fig. 3E. At the beginning, Ce(NO$_3$)$_3$·6H$_2$O and NaF are mixed with the desired amount of NaNO$_3$/KNO$_3$ salts to form a precursor, which is then fired at 350 °C to produce a molten flux. During

the process, the precursor molecules disperse, dissociate, rearrange, and then diffuse rapidly throughout the molten salts to form small nuclei. As the reaction time increases, these nuclei grow into hexagonal-phased CeF$_3$, which are some hexagonal prism nanoparticles (Fig. 3A). The seeds have isotropic unit cell structures, inducing an isotropic growth of particles. When Tb(NO$_3$)$_3$·6H$_2$O was added as raw materials, similar reaction proceeded and Tb^{3+} may substitute for Ce^{3+} in the CeF$_3$ lattice. With the increasing of Tb^{3+} content, the morphology changed (Fig. 3B, C). When the concentration of Tb^{3+} increased to 100%, some orthorhombic phase octahedrons TbF$_3$ achieved (Fig. 3D). The SEM images also reveal the similar results. The shape and size evolution may be caused by the different crystal structures between CeF$_3$ (hexagonal phase) and TbF$_3$ (orthorhombic phase) with different amount of Tb^{3+} ions doped in the CeF$_3$ structure.

Fig. 4A displays the low-resolution TEM image of the as-prepared CeF$_3$ sample, which is composed of hexagonal microprisms and some small grain-like particles, basically corresponding to the SEM observation. The HRTEM image (Fig. 4B) shows obvious lattice fringes, indicating the highly crystalline nature of the CeF$_3$ sample. The interplanar distance between the adjacent lattice planes is determined to be 0.33 nm, agreeing well with the d-spacing value of the (111) planes for the hexagonal phase CeF$_3$. A hexagonal array of spots given in the corresponding fast Fourier- transform diffractogram (FFT) (Fig. 4C) also indicates the hexagonal phase of the CeF$_3$. The chemical composition was scrutinized by EDS analysis (Fig. 4D), which suggests the Ce, F elements in the sample.

3.2. Photoluminescence properties

The luminescent spectra of trivalent lanthanide ions in phosphors mainly compose two types of electronic transitions: 4–4f and 5d–4f
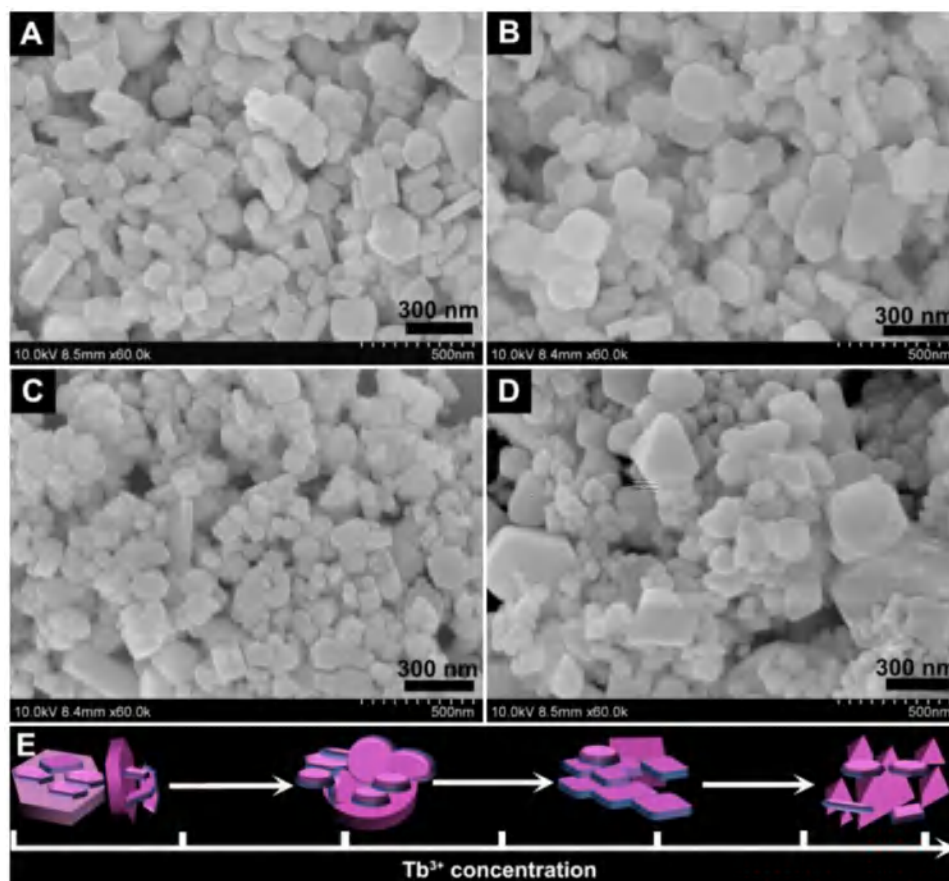
Fig. 3. FE-SEM images of CeF$_3$ (A), CeF$_3$:5%Tb^{3+} (B), CeF$_3$:40%Tb^{3+} (C), TbF$_3$ (D) and the schematic illustration showing the evolution process (E).
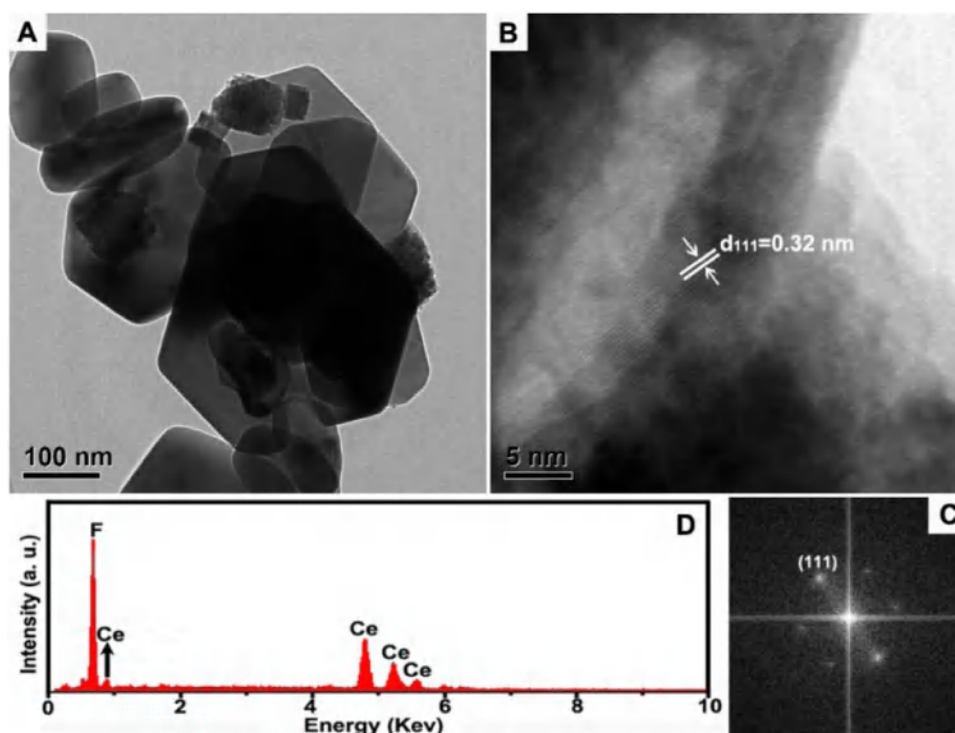
Fig. 4. Low-resolution TEM image (A), HRTEM image (B), corresponding FFT image (C), and the EDS spectrum (D) of the CeF_3 sample.
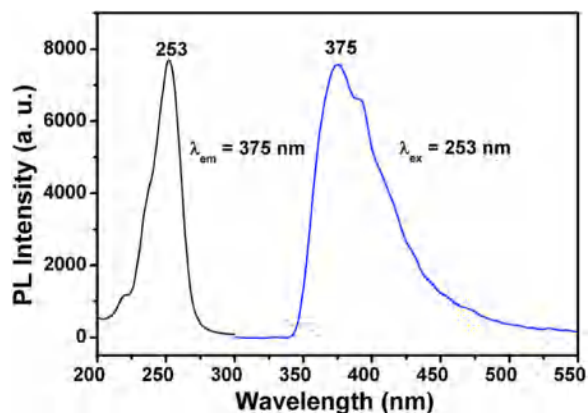
Fig. 5. The excitation (left) and emission (right) spectra of CeF_3 sample.
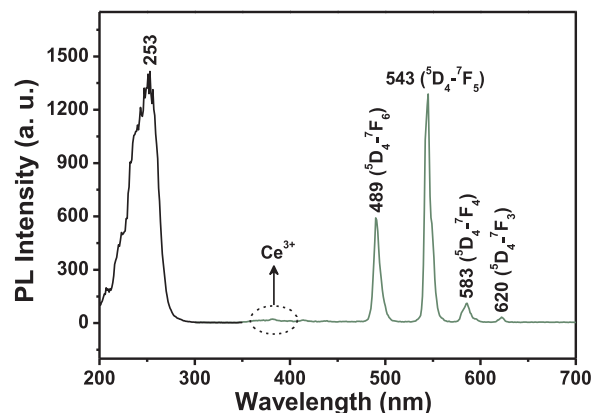
Fig. 6. The excitation (left) and emission (right) spectra of $CeF_3:20\%Tb^{3+}$ sample.

transitions. The former generally shows sharp emission line which is less influenced by the surroundings while the latter has a broad band character. The 4f configuration of Ce^{3+} ion has only one electron, and the irradiation of UV photon will excite this 4f electron into a d orbital, leaving the 4f shell empty. The non-shield outer shell of Ce^{3+} is very sensitive to the host lattices and the emission wavelength depends much on the surroundings. Fig. 5 gives the excitation and emission spectra of CeF_3 sample. The excitation (Fig. 5A, right) monitored at 253 nm, a broad band ranging from 340 to 500 nm with a maximum at 375 nm is observed which is $2000\,cm^{-1}$ due to the ground-state splitting ($^2F_{5/2}$ and $^2F_{7/2}$) which induces two resolved emission peaks. But current split for Ce^{3+} can not be obtained, which may be due to the broadening of spectral lines induced by the small size effects [17].

As the CeF_3 phosphors are doped with Tb^{3+} ions, they exhibit strong green emissions of Tb^{3+} under UV excitation. Fig. 6 shows the excitation and emission spectra of $CeF_3:20\%Tb^{3+}$ sample. The excitation spectrum monitored with the 543 nm emission ($^5D_4–^7F_5$) of Tb^{3+} is identical to that of CeF_3 sample with a maximum at 253 nm. The presence of the Ce^{3+} excitation band suggests the energy transfer from

Ce^{3+} to Tb^{3+}. Excitation into the Ce^{3+} band at 253 nm yields the characteristic $^5D_4–^7F_6$ (489 nm), $^5D_4–^7F_5$ (543 nm), $^5D_4–^7F_4$ (583 nm), and $^5D_4–^7F_3$ (620 nm) transitions of Tb^{3+}, which originate from the f–f transitions within the Tb^{3+} $4f^8$ electron.

Fig. 7 shows the photoluminescence decay curve of the $CeF_3:20\%Tb^{3+}$ sample prepared at 350 °C. The decay curve can be fitted to single exponential functions as $I = I_0 \exp(-t/\tau)$, (I_0 is the initial intensity at t = 0, τ is the 1/e lifetime of the Tb^{3+} ion), from which the lifetime of $CeF_3: 20\%Tb^{3+}$ was determined to be 5.78 ms.

The emission intensity of the $CeF_3:xTb^{3+}$ sample is strongly affected by the doped Tb^{3+} concentration. The emission intensity as a function of the concentration of the doped Tb^{3+} ions is given in Fig. 8. We can see that the emission intensity of Tb^{3+} increases gradually with the Tb^{3+} concentration, reaching a maximum at the doping concentration of 20 mol%. The intensity then decreases, which is opposite to the emission intensity of Ce^{3+}. The doping concentration for Tb^{3+} green emission is optimized to be 20% in $CeF_3:xTb^{3+}$ samples prepared by molten salt route.
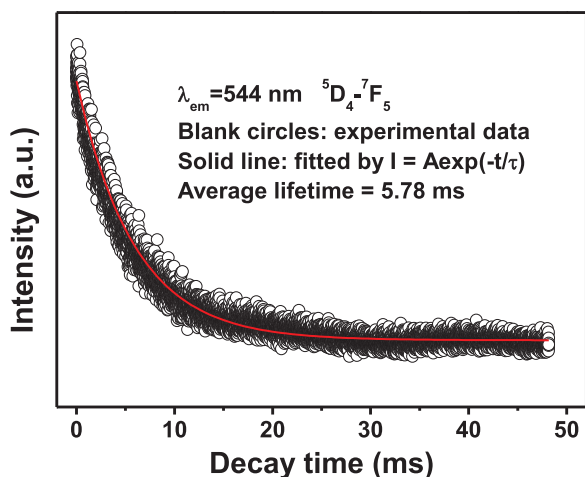
Fig. 7. The luminescence decay curve for CeF$_3$: 20% Tb^{3+} phosphor.
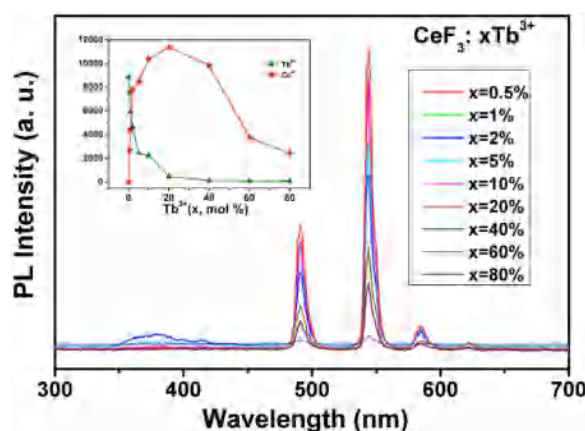
Fig. 8. Effect of Tb^{3+} concentration on the emission intensity of CeF$_3$:xTb^{3+} samples.
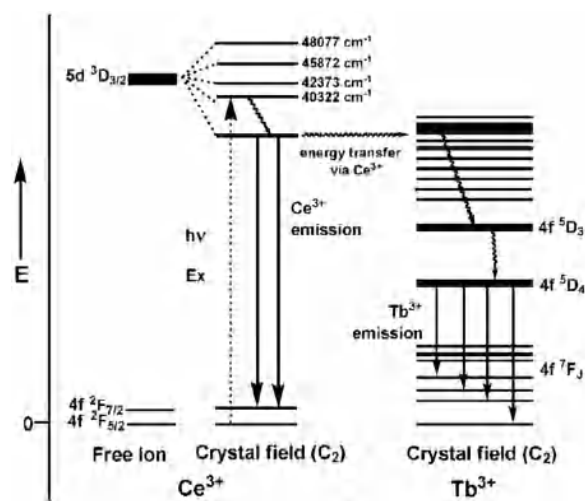
Fig. 9. Energy level scheme of CeF$_3$:Tb^{3+} with electronic transitions and energy transfer processes.

Doping is an efficient way to improve the emission efficiency for solid-state luminescent materials by energy transfer. The 4f^n configurations of Tb^{3+}- related excitation is not efficient due to its spin- and parity-forbidden transitions that the excitation efficiency for Tb^{3+} itself is very low. However, high-light output can be dramatically performed by exciting another ion (sensitizer) with an allowed electronic
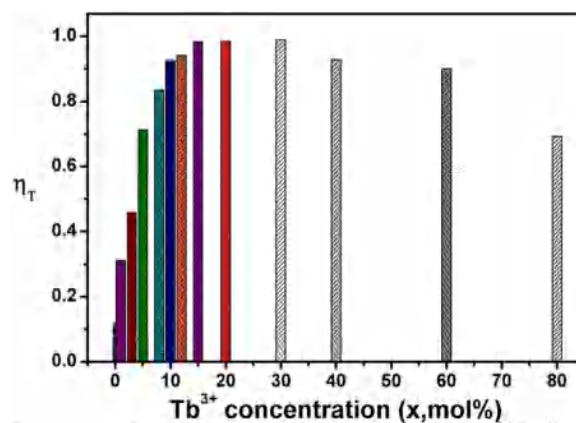
Fig. 10. Room temperature luminescent integral intensity as a function of the Tb^{3+} concentration.

transition which transfers the excitation energy to the rare earth activator. The optically allowed d-f transitions of Ce^{3+} ion serve as an excellent sensitizer for pumping Tb^{3+} emission. Therefore, the strong Tb^{3+} emission peaks can be obtained by excitation of Ce^{3+} ion via an efficient energy transfer from Ce^{3+} to the high excitation levels of Tb^{3+} (4f^8), followed by cross relaxation (Tb^{3+}) can be expressed as the equal of electronic transitions (Ce^{3+}, Tb^{3+}) and energy-transfer processes (Ce^{3+} -Tb^{3+}) are schematically shown in Fig. 9.

Generally, the energy transfer efficiency from a sensitizer to an activator varies with the concentration of activator for the same sensitizer concentration. In our case, Ce^{3+} is the sensitizer and Tb^{3+} is the activator. Fig. 10 shows the results of energy transfer efficiency from Ce^{3+} to Tb^{3+} calculated by above equation at different Tb^{3+} contents. As shown, the energy transfer efficiency increases with increasing Tb^{3+} from 5% to 20%, while the increscent rate of the emission intensity gradually decreases with the increase of Tb^{3+}. The result reveals that the energy transfer from Ce^{3+} to Tb^{3+} tends to saturation with a continuous increase of Tb^{3+} concentration. The decreases with further raise of the Tb^{3+} concentration may be due to the closely spaced ions which lead to deleterious energy migration among Tb^{3+}-Tb^{3+} ions at high concentration. In the energy migration process, the excitation energy will be lost at a killer or quenching site, resulting in the decrease of luminescence efficiency. For CeF$_3$:20%Tb^{3+}, the estimated energy transfer rate is 98.2%, indicating that the energy transfer from Ce^{3+} to Tb^{3+} in CeF$_3$:20%Tb^{3+} is very efficient.

Two main factors are responsible for the resonant energy-transfer from a sensitizer to an activator: one is exchange interaction and the other is multipolar interaction [35]. Exchange interaction needs a large direct or indirect overlap between donor and acceptor orbitals to lead to easy electronic exchange. Although both Ce^{3+} and Tb^{3+} ions are reducing ions, such an exchange would require high energies [36]. Therefore it is impossible for energy transfer to occur through exchange interaction. Thus, in our current system, the energy transfer may take place by means of an electric multipolar interaction. The transition of the Ce^{3+} ions from the 5d excited state to the ^{2}F$_{5/2}$ and ^{2}F$_{7/2}$ ground states are pure electric dipolar transitions, but the 4f^8–4f^8 Tb^{3+} transitions have simultaneously dipolar and quadrupolar character. Therefore, both dipole–dipole and dipole–quadrupole mechanisms may be involved in the energy- transfer from the Ce^{3+} to Tb^{3+} ions [37]. According to Dexter's transfer formula of multipolar interaction and Reisfeld's approximation, the following equation can be given [38,39]:

$$\frac{\eta_0}{\eta} \propto C_{Ce+Tb}^{n/3}$$

in which η_o and η are the luminescence quantum efficiency of Ce^{3+} in the absence and presence of Tb^{3+}; the values of η_o /η can be approximately calculated by the ratio of related luminescence intensities (I_0/I);

C_{Ce+Tb} is the total dopant concentration of Ce^{3+} and Tb^{3+}; and the n = 6, 8, and 10, are dipole–dipole, dipole–quadrupole, and quadrupole–quadrupole interactions, respectively. A linear relationship was only observed when n = 8. This clearly indicates that the energy transfer from the Ce^{3+} to the Tb^{3+} ions is the dipole–quadrupole type interaction. Therefore, the electric dipole–quadrupole interaction predominates in the energy-transfer mechanism from the Ce^{3+} to the Tb^{3+} ions in this system. Considering the dipole-quadrupole interaction, the critical distance from sensitizer to acceptor can also be calculated by the spectral overlap method, as expressed as follows [40]:

$$R_C^8 = 3.024 \times 10^{12} \lambda_S^2 f_q \int \frac{F_S(E)F_A(E)dE}{E^4}$$

where f_q is the oscillator strength of the involved absorption transition of the acceptor (Tb^{3+}). However, there is no concrete value of f_q for Tb^{3+} up to now. It was suggested by Verstegen et al. that the ratio f_q/f_d is about 10^{-3}-10^{-2} when f_d is applied to a forbidden dipole transition. f_d is the oscillator strength of the Tb^{3+} electric dipole transition which is in the order of 10^{-6}. λ_S (in Å) is the wavelength position of the sensitizer's emission. $F_S(E)$ represents the normalized emission shape function of the sensitizer, $F_A(E)$ is the normalized absorption shape function of the activator, and E is the energy involved in the energy transfer process (in eV). $\int F_S(E)F_A(E)dE/E^4$ represents the spectral overlap between the normalized shapes of the Ce^{3+} emission $F_S(E)$ and the Tb^{3+} excitation $F_A(E)$, and in our case it is calculated to be about $0.0154\,eV^{-4}$ and the critical distance R_C was estimated to be 12.65–16.86 Å.

3.3. Cathodoluminescence properties

Under low-voltage electron beam excitation, the cathodoluminescence properties of the CeF_3:Tb^{3+} samples are similar to their photoluminescence properties. In Fig. 11, the representative CL spectra of the CeF_3:20%Tb^{3+} sample **s**hows the characteristic Tb^{3+} emission at 543 nm and 489 nm, which correspond to the Tb^{3+} transitions of $^5D_4$–$^7F_5$, and $^5D_4$–$^7F_6$, respectively. The CL emission intensities of CeF_3:20%Tb^{3+} phosphor has been representatively investigated as a function of the filament current and the accelerating voltage, as shown in Fig. 12. When the filament current is fixed at 85 mA, the CL intensity increases with increasing the accelerating voltage from 2.0 to 4.0 kV (Fig. 12A). Similarly, under a 4.0 kV electron-beam excitation, the CL intensity also increases with increasing the filament current from 85 to 93 mA (Fig. 12B). The increase in CL brightness with an increase in electron energy and filament current is attributed to the deeper penetration of the electrons into the phosphor body and the larger electron-beam current density. The electron penetration depth can be estimated
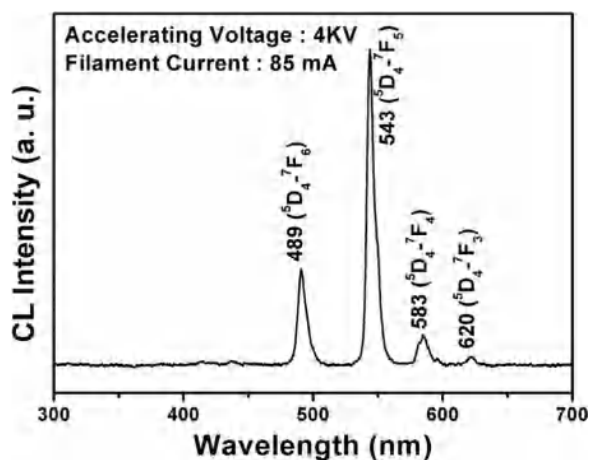
Fig. 11. Typical cathodoluminescence spectrum of CeF_3:20%Tb^{3+} (accelerating voltage, 4 kV; filament current, 85 mA).
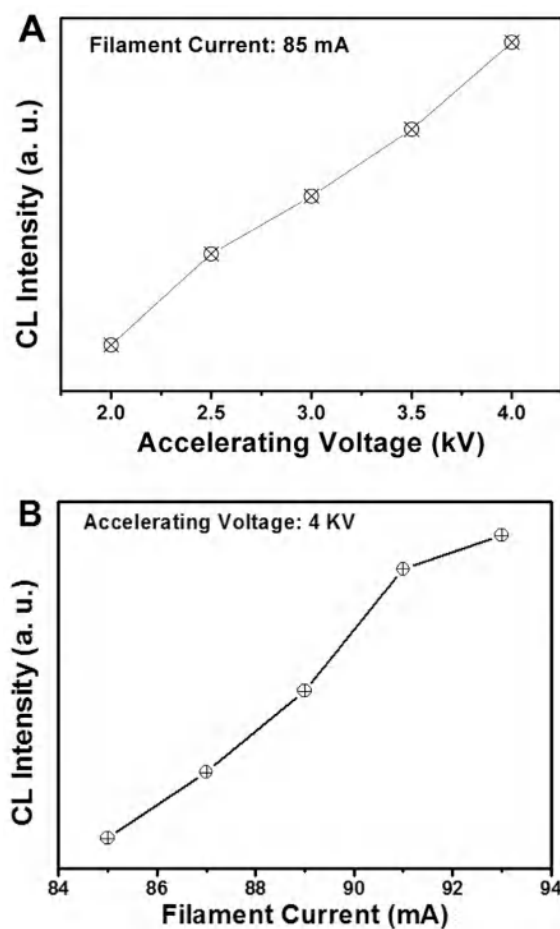
Fig. 12. CL intensity of the CeF_3:20%Tb^{3+} sample as a function of accelerating voltage (A) and filament current (B).

using the empirical formula: $L[A(o)] = 250\ (A/\rho)\ (E/Z^{1/2})^n$, where n = 1.2/(1–0.29logZ) and A is the atomic or molecular weight of the material, F is the bulk density, Z is the atomic number or the number of electrons per molecule in the case compounds, and E is the accelerating voltage (kV) [41]. For CeF_3: 20%Tb^{3+}, Z = 85, A = 197.1, ρ = 6.16 g/cm^3, the estimated electron penetration depth at 4 kV is about 82.2 nm. For cathodoluminescence, the Tb^{3+} ions are excited by the plasma produced by the incident electrons. The deeper the electron penetration depth, the more the plasma will be produced, which resulted in more Tb^{3+} ions being excited and thus the CL intensity increased.

In accordance with the previously describe, the molten-salt synthesis (MSS) method need lower temperatures and often in overall shorter reaction times with little residual impurities as compared with conventional solid-state reactions. As far as we know, few reports describe the process of preparation of rare-earth fluorides in solid reaction may be due to the strict experimental conditions such as fluoride atmosphere. We try to prepare it using solid state method at 800 °C in the N_2 atmosphere. The corresponding XRD pattern in Fig. S1 validates the bad crystallization the product, the impurity phase of CeO_2 occupy the major part. Our group have prepared the CeF_3 phosphors by hydrothermal/solvothermal process [42], however, they usually suffers from the low yield and long reaction time reaction. In addition, the required toxic organometallic precursors and/or the corrosive acid used in the thermolysis method have become matters of substantial environmental concern. Due to the different synthesis condition, different shape and size of samples, it dose not make much sense to compare the luminescence properties and the results are not shown here.

4. Conclusions

Well crystalline CeF_3 and CeF_3:Tb^{3+} phosphors were prepared by a facile and mass-production low temperature molten salt process. The substitution of Tb^{3+} for Ce^{3+} in the CeF_3 lattice induces the transformation of the phase, size, morphology and also affects the luminescent properties of the samples. CeF_3 phosphors have a strong UV emission from Ce^{3+} and CeF_3:Tb^{3+} show strong green emissions from Tb^{3+}. The energy transfer mechanism from Ce^{3+} to Tb^{3+} in CeF_3:Tb^{3+} was well investigated and the critical distance was estimated. The calculated data reveal that the transfer is very efficient. The optimal doping concentration for Tb^{3+} green emission is 20%Tb^{3+} in CeF_3:xTb^{3+} particles. The cathodoluminescence property of CeF_3:Tb^{3+} phosphor shows the characteristic emissions of Tb^{3+} which is similar to the photoluminescence properties. The outstanding luminescence intensity and efficient energy transfer make it highly potential in the field of solid state light emitting materials.

Appendix A. Supporting information

Supplementary data associated with this article can be found in the online version at https://doi.org/10.1016/j.jlumin.2018.08.067.

References

[1] H.A. Hoeppe, Recent developments in the field of inorganic phosphors, Angew. Chem.-Int Ed. 48 (2009) 3572–3582.

[2] Z.W. Pan, Z.R. Dai, Z.L. Wang, Nanobelts of semiconducting oxides, Science 291 (2001) 1947–1949.

[3] A.D.J. David, G.S. Muhammad, V. Sivakumar, Synthesis and photoluminescence properties of Sm^{3+} substituted glaserite-type orthovanadates $K_3Y[VO_4]_{(2)}$ with monoclinic structure, J. Lumin. 177 (2016) 104–110.

[4] D. Li, Q. Ma, Y. Song, X. Xi, X.T. Dong, W.S. Yu, J. Wang, G.X. Liu, NaGdF4:Dy^{3+} nanofibers and nanobelts: facile construction technique, structure and bifunctionality of luminescence and enhanced paramagnetic performances, Phys. Chem. Chem. Phys. 18 (2016) 27536–27544.

[5] D. Li, Q. Ma, Y. Song, X. Xi, X.T. Dong, W.S. Yu, J. Wang, G.X. Liu, Tunable multicolor luminescence and white light emission realized in Eu^{3+} mono-activated GdF3 nanofibers with paramagnetic performance, RSC Adv. 6 (2016) 113045–113052.

[6] M. Shang, G. Li, X. Kang, D. Yang, D. Geng, J. Lin, Tunable luminescence and energy transfer properties of Sr_3AlO_4F: RE^{3+} (RE = Tm/Tb, Eu, Ce) phosphors, ACS Appl. Mater. Interfaces 3 (2011) 2738–2746.

[7] G. Li, D. Geng, M. Shang, C. Peng, Z. Cheng, J. Lin, Tunable luminescence of Ce^{3+}/Mn^{2+}-coactivated $Ca_2Gd_8(SiO_4)6O_2$ through energy transfer and modulation of excitation: potential single-phase white/yellow-emitting phosphors, J. Mater. Chem. 21 (2011) 13334–13344.

[8] D. Li, Q.L. Ma, X. Xi, X.T. Dong, W.S. Yu, J. Wang, G.X. Liu, Dy^{3+} and Eu^{3+} Co-doped NaGdF4 nanofibers endowed with bifunctionality of tunable multicolor luminescence and paramagnetic properties, Chem. Eng. J. 309 (2017) 230–239.

[9] J. Gu, Z.Q. Zhao, Y. Ding, H.L. Chen, Y.W. Zhang, C.-H. Yan, Liquid-phase syntheses and material properties of two-dimensional nanocrystals of rare earth-selenium compound containing planar Se layers: $RESe_2$ nanosheets and $RE_4O_4Se_3$ nanoplates, J. Am. Chem. Soc. 135 (2013) 8363–8371.

[10] D. Li, X.T. Dong, W.S. Yu, J. Wang, G.X. Liu, Synthesis and upconversion luminescence properties of YF3:Yb^{3+}/Er^{3+}, hollow nanofibers derived from Y_2O_3:Yb^{3+}/Er^{3+} hollow nanofibers, ,J. Nanopart. Res. 15 (2013) 1704.

[11] A. Maaoui, M. Haouari, A. Bulou, B. Boulard, H. Ben Ouada, Effect of BaF_2 on the structural and spectroscopic properties of Er^{3+}/Yb^{3+} ions codoped fluoro-tellurite glasses, J. Lumin. 196 (2018) 1–10.

[12] S.Y. Min, J. Bang, J. Park, C.L. Lee, S. Lee, J.J. Park, U. Jeong, S. Kim, T.W. Lee, Electrospun polymer/quantum dot composite fibers as down conversion phosphor layers for white light-emitting diodes, RSC Adv. 4 (2014) 11585–11589.

[13] K. Schmalzl, D. Strauch, Static Pockels constants p(ij) and p(ijk) of CaF_2 and BaF_2 under strain from ab initio calculations, Phys. Rev. B 76 (2007) 205106.

[14] D. Li, Q. Ma, Y. Song, X. Xi, X.T. Dong, W.S. Yu, J. Wang, G.X. Liu, Novel strategy to

[15] achieve NaGdF4:Eu^{3+} nanofibers with color-tailorable luminescence and paramagnetic performance, J. Am. Ceram. Soc. 100 (2017) 2034–2044.

[15] R.X. Yan, Y.D. Li, Down/Up conversion in Ln^{3+}-doped YF3 nanocrystals, Adv. Funct. Mater. 15 (2005) 763–770.

[16] M.C. Tan, G.A. Kumar, R.E. Riman, Near infrared-emitting Er and Yb/Er doped CeF_3 nanoparticles with no visible upconversion, Opt. Express 17 (2009) 15904–15910.

[17] S.F. Zou, Z.L. Zhang, F. Zhang, Y.L. Mao, High efficient quantum cutting in Ce^{3+}/Yb^{3+} co-doped oxyfluoride glasses, J. Alloy. Compd. 572 (2013) 110–112.

[18] Y. Zhou, D. Chen, W. Tian, Z. Ji, Impact of Eu^{3+} dopants on optical spectroscopy of Ce^{3+}: $Y_3Al_5O_{12}$-embedded transparent glass-ceramics, J. Am. Ceram. Soc. 98 (2015) 2445–2450.

[19] S.R. Naik, T. Shripathi, A.V. Salker, Preparation, characterization and photoluminescent studies of Cr and Nd co-doped Ce:YAG compounds, J. Lumin. 161 (2015) 335–342.

[20] P. Song, C.M. Zhang, P.F. Zhu, Efficiency stokes shifting luminescent materials: Ce^{3+}-Tb^{3+}-Eu^{3+} toward solar energy applications, Ceram. Int. 42 (2016) 11417–11421.

[21] G. Chen, J. Shen, T.Y. Ohulchanskyy, N.J. Patel, A. Kutikov, Z. Li, J. Song, R.K. Pandey, H. Agren, P.N. Prasad, G. Han, (alpha-NaYbF4:Tm^{3+})/CaF2 core/shell nanoparticles with efficient near-infrared to near-infrared upconversion for high-contrast deep tissue bioimaging, ACS Nano 6 (2012) 8280–8287.

[22] X. Li, Y. Zhang, D. Geng, J. Lian, G. Zhang, Z. Hou, J. Lin, CaGdAlO4:Tb^{3+}/Eu^{3+} as promising phosphors for full-color field emission displays, J. Mater. Chem. C 2 (2014) 9924–9933.

[23] D. Yang, G. Li, X. Kang, Z. Cheng, Pa Ma, C. Peng, H. Lian, C. Li, J. Lin, Room temperature synthesis of hydrophilic $Ln^{(3+)}$-doped KGdF4 (Ln = Ce, Eu, Tb, Dy) nanoparticles with controllable size: energy transfer, size-dependent and color-tunable luminescence properties, Nanoscale 4 (2012) 3450–3459.

[24] T. Lyu, P. Dorenbos, Charge carrier trapping processes in lanthanide doped LaPO4, GdPO4, YPO4, and LuPO4, J. Mater. Chem. C 6 (2018) 369–379.

[25] Y. Zhu, Z. Sun, Z. Yin, H. Song, W. Xu, Y. Wang, L. Zhang, H. Zhang, Self-assembly, highly modified spontaneous emission and energy transfer properties of LaPO4:Ce^{3+}, Tb^{3+} inverse opals, Dalton Trans. 42 (2013) 8049–8057.

[26] S.Y. Kim, K. Woo, K. Lim, K. Lee, H.S. Jang, Highly bright multicolor tunable ultrasmall beta-Na(Y,Gd)F4:Ce,Tb,Eu/beta-NaYF4 core/shell nanocrystals, Nanoscale 5 (2013) 9255–9263.

[27] A.A. Ansari, Influence of surface functionalization on structural and photo-luminescence properties of CeF_3:Tb nanoparticles, Appl. Surf. Sci. 409 (2017) 285–290.

[28] Z.Y. Ma, Y.P. Liu, L.Y. Bai, J. An, L. Zhang, Y. Xuan, X.-S. Zhang, Y.-D. Zhao, Folic acid-targeted magnetic Tb-doped CeF_3 fluorescent nanoparticles as bimodal probes for cellular fluorescence and magnetic resonance imaging, Dalton Trans. 44 (2015) 16304–16312.

[29] S. Liu, Y. Hui, L. Zhu, X. Fan, B. Zou, X. Cao, Synthesis and luminescence properties of CeF_3:Tb^{3+} nanodisks via ultrasound assisted ionic liquid method, J. Rare Earth 32 (2014) 508–513.

[30] S. Varun, M. Kalra, M. Gandhi, White light emission through downconversion of terbium and europium doped CeF_3 nanophosphors, J. Fluoresc. 25 (2015) 1501–1505.

[31] T. Plachy, M. Mrlik, Z. Kozakova, P. Suly, M. Sedlacik, V. Pavlinek, I. Kuritka, The electrorheological behavior of suspensions based on molten-salt synthesized lithium titanate nanoparticles and their core-shell titanate/urea analogues, ACS Appl. Mater. Interfaces 7 (2015) 3725–3731.

[32] B. He, W.-C. Li, A.-H. Lu, High nitrogen-content carbon nanosheets formed using the Schiff-base reaction in a molten salt medium as efficient anode materials for lithium-ion batteries, J. Mater. Chem. A 3 (2015) 579–585.

[33] M.V. Reddy, L.Y. Tse, W.K.Z. Bruce, B.V.R. Chowdari, Low temperature molten salt preparation of nano-SnO2 as anode for lithium-ion batteries, Mater. Lett. 138 (2015) 231–234.

[34] A. Tyminski, T. Grzyb, Are rare earth phosphates suitable as hosts for upconversion luminescence Studies on nanocrystalline REPO4 (RE=Y, La, Gd, Lu) doped with Yb^{3+} and Eu^{3+}, Tb^{3+}, Ho^{3+}, Er^{3+} or Tm^{3+} ions, J. Lumin. 181 (2017) 411–420.

[35] A.A. Ansari, A.K. Parchur, B. Kumar, S.B. Rai, Influence of shell formation on morphological structure, optical and emission intensity on aqueous dispersible NaYF4:Ce/Tb nanoparticles, J. Fluoresc. 26 (2016) 1151–1159.

[36] Z.Y. Ma, Y.P. Liu, L.Y. Bai, J. An, L. Zhang, Y. Xuan, X.-S. Zhang, Y.-D. Zhao, Folic acid-targeted magnetic Tb-doped CeF_3 fluorescent nanoparticles as bimodal probes for cellular fluorescence and magnetic resonance imaging, Dalton Trans. 44 (2015) 16304–16312.

[37] S. Liu, Y. Hui, L. Zhu, X. Fan, B. Zou, X. Cao, Synthesis and luminescence properties of CeF_3:Tb^{3+} nanodisks via ultrasound assisted ionic liquid method, J. Rare Earth 32 (2014) 508–513.

[38] R. Reisfeld, E. Greenberg, R. Velapoldi, B. Barnett, Luminescence quantum efficiency of Gd and Tb in borate glasses and the mechanism of energy transfer between them, J. Chem. Phys. 56 (1972) 1698–1705.

[39] D.L. Dexter, J.H. Schulman, Theory of concentration quenching in inorganic phosphors, J. Chem. Phys. 22 (1954) 1063–1070.

[40] J.M.P.J. Verstegen, J.L. Sommerdijk, J.G. Verriet, Cerium and terbium luminescence in LaMgAl 11 O 19, J. Lumin. 6 (1973) 425–431.

[41] C. Feldman, Range of 1−10 kev electrons in solids, Phys. Rev. 117 (1960) 455–459.

[42] C. Li, X. Liu, P. Yang, C. Zhang, A.H.Z. Lian, J. Lin, LaF3, CeF_3, CeF_3:Tb^{3+} and CeF_3:Tb^{3+}@LaF3 (Core−Shell) nanoplates: hydrothermal synthesis and luminescence properties, J. Phys. Chem. C 112 (2009) 2904–2910.